Anomalous resistivity near the ferroelectric phase transition in (Pb,Ge,Sn)Te alloy semiconductors

S. Takaoka and K. Murase
Department of Physics, Osaka University, Toyonaka, 560 Japan
(Received 1 March 1979)

The phase transition in $Pb_{1-x}Ge_xTe$ ($0 < x < 0.10$) and $Pb_{1-x}Sn_xTe$ has been systematically investigated by the electrical-transport method. The composition dependence of the transition temperature in $Pb_{1-x}Ge_xTe$ determined from an electrical resistivity anomaly is in good agreement with other experiments. We found that the resistivity-anomaly peak position increases with a reduction of the anomaly under a strong magnetic field in $Pb_{1-x}Ge_xTe$ ($x = 0.01, 0.015$) and $Pb_{1-x}Sn_xTe$ ($x = 0.40$). The magnetic field dependence is tentatively explained by an interband-electron–TO-phonon coupling model, taking into account the phonon anharmonicity.

I. INTRODUCTION

Recently PbTe-GeTe-SnTe alloy semiconductors have been extensively studied for application to wavelength-tunable infrared detectors[1] and lasers.[2] Both electronic and lattice properties have been investigated in cooperation with basically important works such as determination of phase diagrams[3,4] and developments of the crystal-growth technique.[5] The $Pb_{1-x}Ge_xTe$ and $Pb_{1-x}Sn_xTe$ systems exhibit a structural phase transition from a high-temperature NaCl-to a low-temperature As-type structure in alloy composition ranges with more than 1 at.% Ge or 35 at.% Sn. There have been many experimental studies of the structural phase transition by Raman scattering,[6–8,24] electrical-resistivity measurement,[8–11] neutron scattering,[12,13] x-ray diffraction,[4,14] capacitance measurement of p-n junction,[15,16] ultrasonic attenuation and velocity,[17] and magnetoplasma reflection,[18,19] etc. A considerable attention has been paid to an apparent carrier-concentration dependence of the transition temperature (T_c)[11] and to the soft TO-phonon mode frequencies.[7] These phenomena have been explained on the basis of an interband-electron–TO-phonon coupling model[20,21] taking into account the anharmonic phonon-phonon interactions.

In this paper, we have investigated electric-transport properties in order to understand microscopically the phase transition of $Pb_{1-x}Ge_xTe$ and $Pb_{1-x}Sn_xTe$. We found an anomalous increment of the resistivity near T_c in these systems. We determined T_c systematically for many specimens with different Ge compositions ($0 < x < 0.10$). Under a strong magnetic field we observed a significant change of a resistivity peak position accompanying a reduction of the anomalous increment. The magnetic-field effects were tentatively analyzed by the interband-electron–TO-phonon coupling model. We can explain a change in T_c based on this model, since the interband coupling strength should change through magnetic quantization of the electrons in a strong magnetic field.[8] In Sec. II, we will describe experiments in detail and present our experimental data. The experimental analysis and discussion of the magnetic-field dependence will be presented in Sec. III on the basis of the interband-electron–TO-phonon coupling model. A summary and concluding remarks will be given in Sec. IV.

II. EXPERIMENTAL DETAILS

A. Sample preparation

The samples were prepared by a vapor-transport method to get large homogeneous single crystals.[5] The carrier concentrations were controlled by changing the growth temperature in $Pb_{1-x}Ge_xTe$ ($x = 0.01, 0.015$) or by isothermal annealing in $Pb_{1-x}Sn_xTe$.[3] In Table I and II we list carrier concentrations and mobilities determined from Hall measurements, T_c, and crystal-growth conditions. The grown crystals were cut by a spark cutter. Slices were etched in a H_2O-KOH-$C_2H_8O_3$ (20:20:1) solution or in concentrated HBr with a drop of 30-vol%-H_2O_2 solution to remove surface damages. The typical size of the samples was $6 \times 1 \times 1$ mm^3 in $Pb_{1-x}Ge_xTe$ and was $4 \times 0.6 \times 0.3$ mm^3 in annealed $Pb_{1-x}Sn_xTe$.

B. Experimental procedure

The electrical resistivity ρ and the Hall coefficient R were measured using standard dc techniques. Four voltage probes with 50-μm platinum wires were attached to a sample by an electrical discharge method with a typical sparking voltage of 10–15 V. The two current-probe wires were soldered with Indoalloy No. 2 or 5 or attached by sparking. A good ohmic contact was not easy to obtain for low-carrier-concentration

TABLE I. Characteristics of $Pb_{1-x}Ge_xTe$ samples.

x (%)	n,p (10^{18} cm^{-3})	Crystal growth	μ_H(77 K) (cm^{2}V^{-1}sec^{-1})	μ_H(4.2 K) (cm^{2}V^{-1}sec^{-1})	T_c[d] (K)	$\Delta\rho(T_c)$[e] (Ω cm)
0.0	n, 0.11	v.t.[b] (850 °C)	4.3×10^4	52×10^4	···	···
0.5	n, 0.14	v.t. (830 °C)	2.4×10^4	58×10^4	···	···
1.0	p, 0.61	v.t. (830 °C)	2.0×10^4	5.2×10^4	23.6	4.4×10^{-5}
1.0	n, 3.7	v.t. (790 °C)	1.4×10^4	3.8×10^4	16.5	···
1.0	p, 2.9	v.t. (795 °C)	7.6×10^3	3.5×10^4	39.4	5.2×10^{-5}
1.0	p, 2.6	v.t. (820 °C)	1.3×10^4	4.5×10^4	33.5	4.7×10^{-5}
1.0	n, 0.72	v.t. (810 °C)	2.4×10^4	8.4×10^4	22	···
1.0	n, 0.30	v.t. (820 °C)	4.9×10^4	22×10^4	33.5	7.4×10^{-5}
1.0	p, 0.17	v.t. (830 °C)	4.0×10^4	17×10^4	32.8	9.2×10^{-5}
1.0	n, 0.45	v.t. (826 °C)	2.1×10^4	4.5×10^4	23.5	···
1.0	p, 0.48	v.t.s.[c] (800 °C)	1.5×10^4	6.5×10^4	36	6.2×10^{-5}
1.25	n, 0.33	v.t. (830 °C)	2.5×10^4	5.4×10^4	···	···
1.5	p, 1.33	v.t. (790 °C)	1.3×10^4	6.3×10^4	47	7.5×10^{-5}
1.5	n, 0.79	v.t. (790 °C)	2.1×10^4	5.3×10^4	51.5	7.7×10^{-5}
1.5	p, 0.65	v.t. (792 °C)	3.0×10^3	4.1×10^4	47	···
1.5	p, 0.29	v.t. (800 °C)	···	···	52	···
1.5	n, 0.28	v.t. (791 °C)	···	···	···	···
1.5	n, 0.54	v.t.s. (795 °C)	2.1×10^4	6.2×10^4	50.3	1.1×10^{-4}
2.0	p, 1.8	v.t. (770 °C)	1.0×10^4	2.7×10^4	70.5	3.2×10^{-5}
2.0	p, 0.90	v.t. (780 °C)	1.5×10^4	6.9×10^4	62.2	1.1×10^{-4}
3.0	p, 2.4	v.t. (800 °C)	6.6×10^3	···	100.5	7.6×10^{-5}
3.1[a]	p, 2.4	Bridgeman	3.6×10^3	···	105	1.1×10^{-5}
4.0[a]	p, 3.6	Bridgeman	3.1×10^3	···	119	7.7×10^{-5}
5.5[a]	p, 4.0	v.t. (817 °C)	0.8×10^3	···	143	2.4×10^{-4}
5.5[a]	p, 0.85	v.t. +annealing (550 °C)	2.9×10^3	···	149	2.6×10^{-4}
5.5[a]	p, 4.2	v.t.s. (830 °C)	2.4×10^3	···	143.5	1.5×10^{-4}
7.0	p, 3.2	v.t. (800 °C)	5×10^2	···	163	2.6×10^{-4}
10.0	p, 3.2	v.t. (800 °C)	1.7×10^2	···	223	3.3×10^{-4}

[a]Determined from the lattice constant.
[b]v.t.: vapor transport.
[c]v.t.s.: v.t. with seed.
[d]T_c: from the resistivity anomaly.
[e]$\Delta\rho(T_c)$: magnitude of resistivity anomaly at T_c.

samples with carriers of less than about 10^{17} cm^{-3}. Resistivities and Hall coefficients were measured with a temperature-controlled cryostat by changing the heater current. Sample temperatures were measured with a Au + 0.07 at.% Fe–chromel thermocouple (Osaka Sanso Co., Ltd.) over the range from 4.2 to 300 K. The sample was glued to a copper block with Apiezon grease *N*. The current direction was usually parallel to a ⟨100⟩ direction. Resistivities were measured with a temperature changing rate of about 0.5 K/min. A magnetic field was applied along the current by a superconducting magnet up to 90 kG, in most of the resistivity measurements. A more strong magnetic field up to 150 kG [by the Intermagnetics General Corporation magnet at the Institute of Solid State Physics (Tokyo)] was applied on some samples: the thermocouple output is not practically influenced by a magnetic field up to 150 kG within 0.1 K. Hall measurements were usually performed in a magnetic field of 20 kG at 4.2 and 77 K.

C. Experimental results

We measured the temperature dependence of the resistivity in $Pb_{1-x}Ge_xTe$ with various x up to 10%. An anomalous hump was observed in the resistivity near T_c. Typical examples are shown in Fig. 1(a) to 1(c) for p-type samples. Similar results were obtained for n-type samples ($x = 0.01$ and 0.015) as shown in Fig. 1(d). In fact there is no resistivity anomaly in PbTe, which does not transform at finite temperature as shown in Fig. 1(e).

In Fig. 2 we plotted the peak position of the resis-

TABLE II. Characteristics of $Pb_{1-x}Sn_xTe$ samples.

x (%)	p (10^{18} cm^{-3})	Crystal growth	μ_H^a (77 K) (cm^{2}V^{-1}sec^{-1})	μ_H (4.2 K) (cm^{2}V^{-1}sec^{-1})	$T_c^b(K)$
35	0.68	v.t.[c]+annealing (450 °C)	1.4×10^4	4.3×10^4	12
40	7.4	v.t.+annealing (600 °C)	3.9×10^3	6.3×10^4	22
40	1.1	v.t.+annealing (450 °C)	2.4×10^4	5.4×10^4	17.5
40	0.71	v.t.+annealing (425 °C)	2.2×10^4	5.1×10^4	19
40[d]	1.2	v.t.(Bi-doped) (750 °C)	1.8×10^4	2.8×10^4	12.5
70	280	v.t.(780 °C)	3.4×10^2	4.7×10^2	44

[a] μ_H: Hall mobility at 77 and 4.2 K.
[b] T_c: from resistivity anomaly.
[c] v.t.: vapor transport.
[d] Supplied by R. Kawabata, otherwise from S. Nishi.

tivity anomaly with different Ge compositions (x) together with other experimental results (x-ray diffraction,[4] capacitance measurement of p-n junction,[16] ultrasonic attenuation,[17] and microwave magnetoplasma reflection). As the agreement between the peak positions and other experiments is very good, one may assign a peak position to a transition temperature. We found that the peak position of the anomaly in $Pb_{1-x}Ge_xTe$ shifts to the high-temperature side along with a reduction of its peak height by application of a strong magnetic field in the ⟨100⟩ direction. Typical data are shown in Fig. 3. We will assume that the peak position corresponds to T_c even under the magnetic field. The magnetic-field dependences of the peak positions are shown for different specimens ($x=0.01$ and 0.015) with various carrier concentrations in Fig. 4. It should be noted that the increment of the peak position (T_c) with application of the magnetic field becomes appreciable above the quantum limit. Similar results were obtained in $Pb_{1-x}Sn_xTe$ ($x=0.40$). However the magnetic-field dependence is slightly different between these alloy systems. The peak position (T_c) decreases at first and then rapidly increases above the quantum limit in $Pb_{1-x}Sn_xTe$ ($x=0.40$) as shown in Figs. 5 and 6. The solid curves in Figs. 4 and 6 are the calculated ones as will be mentioned in detail in Sec. III.

Figure 7 shows the temperature dependence of the resistivity for three different magnetic-field directions in low-carrier-concentration $Pb_{1-x}Ge_xTe$ ($x=0.01$). In Fig. 8 we plot the shifts of the peak positions (T_c) from the values at the zero field and the peak heights of the anomalies normalized by the value at zero field as a function of the magnetic field. The increments of the peak position (T_c) become increasingly small in the ⟨100⟩, ⟨110⟩, and ⟨111⟩ directions. The resistivity anomalies in the ⟨111⟩ direction do not become small compared with those in other directions in the quantum limit. In the $Pb_{1-x}Ge_xTe$ sample ($x=0.015$, $p=1.3\times10^{18}$ cm^{-3}), the anomaly does not become so small even in a ⟨100⟩ configuration.

The Hall coefficients in $Pb_{1-x}Ge_xTe$ ($x=0.01$ and 0.015) do not change appreciably in the temperature range from 4.2 to 100 K within experimental errors. From these facts, one may judge that there is no appreciable change of total carrier concentration and no important mobility difference between the four energy-band valleys under crystal distortion below T_c, and no other carrier contribution such as from near the Σ point in $Pb_{1-x}Sn_xTe$.[22] The resistivity increases well below T_c under a high magnetic field in small-carrier-concentration samples as shown in Fig. 7. If there is a multidomain structure below T_c, such behavior can be expected. The situation of a valley nonequivalency is different for different domains which cause a large increment of electrical resistivity in specimens with small Fermi energies (small carrier concentrations). The magnetoresistance also becomes large in such inhomogeneous valley structures below T_c.

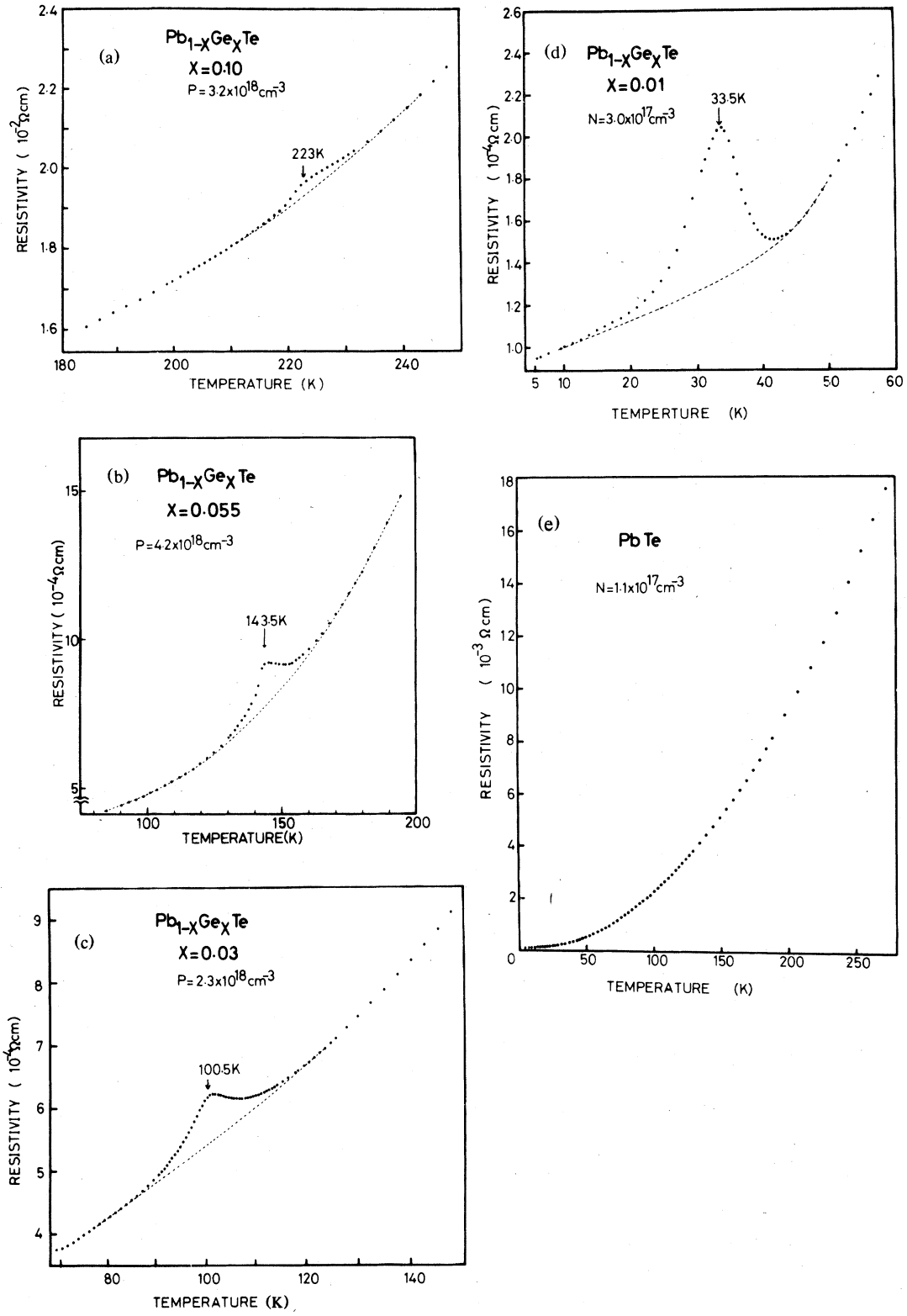

FIG. 1. Temperature dependence of resistivity in $Pb_{1-x}Ge_xTe$: (a) $x=0.10$; (b) $x=0.055$; (c) $x=0.03$; (d) $x=0.01$; (e) $x=0$.

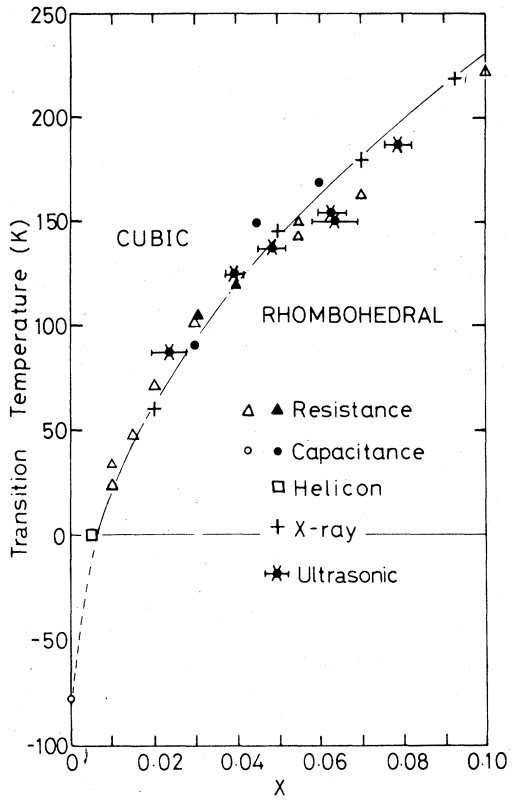

FIG. 2. Transition temperature of $Pb_{1-x}Ge_xTe$ vs Ge content determined from resistivity anomalies with other experiments (the symbol □ denotes the temperature obtained by us by extrapolation according to the Curie-Weiss law with 50-GHz magnetoplasma reflection).

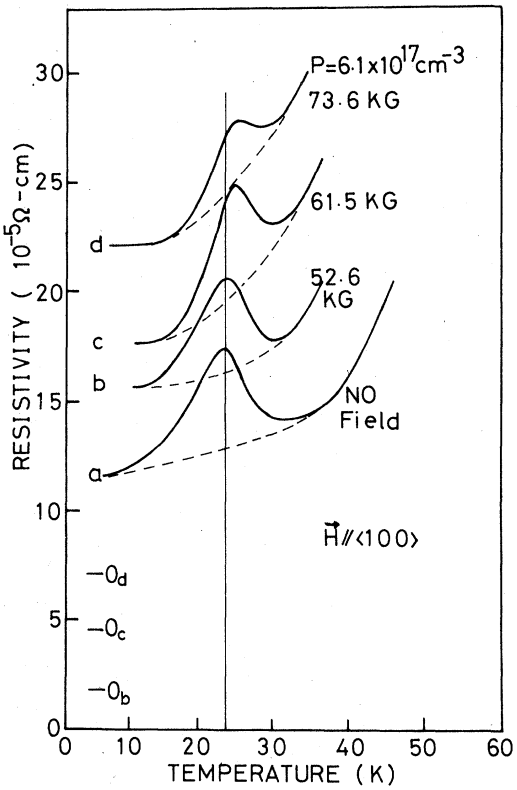

FIG. 3. Resistivity anomalies of $Pb_{1-x}Ge_xTe$ ($x=0.01$) under magnetic field. The peak of the anomaly moves upward in temperature with the magnetic field. 0_b, 0_c, 0_d are the zero points for curves *b*, *c*, and *d*, respectively.

III. EXPERIMENTAL ANALYSES AND DISCUSSION

First, we briefly discuss the origin of the resistivity anomaly. Next, we examine the magnetic-field dependence of T_c through the electron–TO-phonon coupling model by considering the magnetic-field dependence of soft TO modes.

A. Resistivity anomaly near T_c

The increment of the electrical resistivity near T_c has been mainly attributed to an increase of the relaxation rate due to soft TO phonons and screened LO phonons (L^-) through the increment of the Bose factor.[8,10,23] In Fig. 9, the solid curve shows the observed anomaly, which is obtained by subtracting the background contribution [dotted curve in Fig. 1(b)] from the data. We supposed that the background resistivity changes smoothly, since there is no appreciable change in Hall coefficients near T_c. The dotted curve in Fig. 9 shows the theoretical calculation[8] using the formula in Ref. 23. There is a tendency of the magnitude of the resistivity anomaly ($\Delta\rho$) to decrease with decreasing Ge composition x (or T_c) and increasing carrier concentration as shown in Table I. This can be also explained qualitatively by the above model.[23]

B. Magnetic-field dependence of T_c

To examine the magnetic-field dependence of T_c, we start from a soft-TO-phonon expression based on the interband-TO-phonon coupling model taking into account the fourth-order phonon anharmonicity, since the order parameter of the phase transition corresponds to the static shift of the TO-phonon motion and the phase transition is characterized by the soft-TO mode.

The TO-phonon frequency of the above-mentioned model is expressed as[7,9]

$$\tilde{\omega}_{TO}^2=\omega_{TO}^2+\tfrac{1}{2}\alpha_\infty\left(\frac{T}{\Theta}\right)^2 G\left(\frac{\Theta}{T}\right)$$

$$-\frac{2}{MNa^2}\sum_k|\Xi(k)|^2\frac{f(E_{vk})-f(E_{ck})}{E_{ck}-E_{vk}}\ , \qquad (3.1)$$

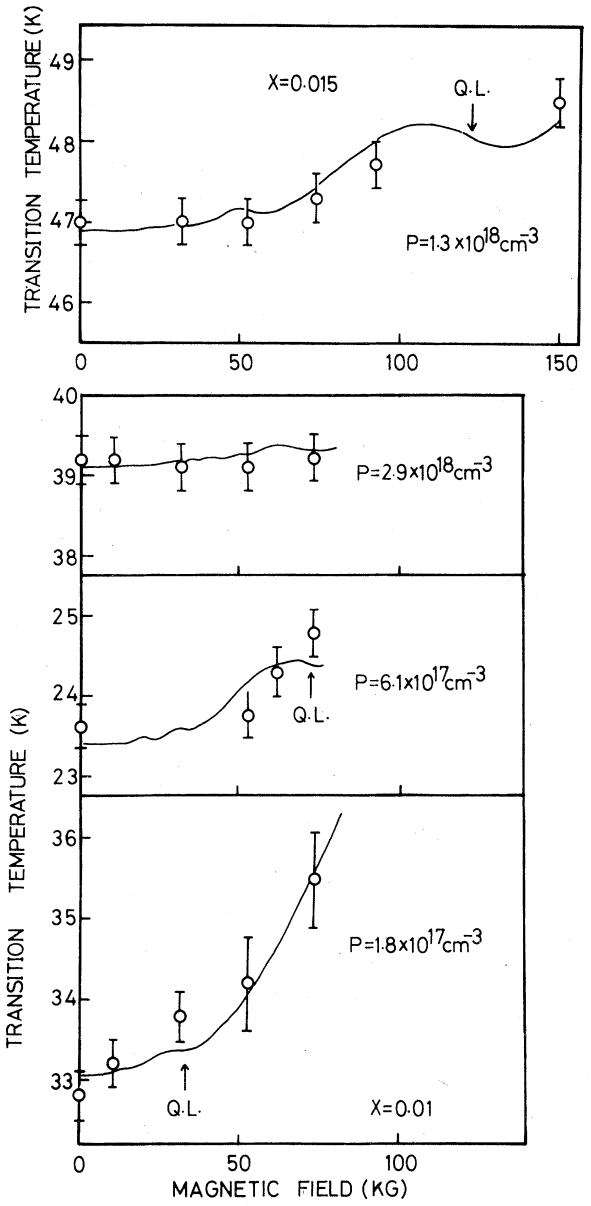

FIG. 4. Transition temperature vs magnetic field in $Pb_{1-x}Ge_xTe$ ($x=0.01$, 0.015) with various carrier concentrations. The open circles are obtained from the resistivity anomalies. Arrows indicate the critical magnetic field of the quantum limit (QL). The solid curves are obtained from the calculation (see text).

with

$$G\left(\frac{\Theta}{T}\right)=\int_0^{\Theta/T} x\coth\left(\tfrac{1}{2}x\right)dx \ ,$$

where α_∞ is the temperature coefficient of the squared TO-phonon frequency at the high-temperature limit and other notations are the same as in Ref. 7. The temperature dependence of the TO-phonon frequency mainly comes from the phonon anharmonic term [the second term of Eq. (3.1)]. Under a magnetic field, the TO-phonon frequency may be modified through a change of the third term in Eq. (3.1). Here we suppose that the third term is divided into two parts. One is a summation near the band edges, and we define the summation as containing the N_T electrons states. The other is the magnetic-field-nondependent term which comes from the remaining part of the electronic bands. When a magnetic field is applied along a ⟨100⟩ direction for an n-type sample with carrier concentration N_c, the term may be rewritten

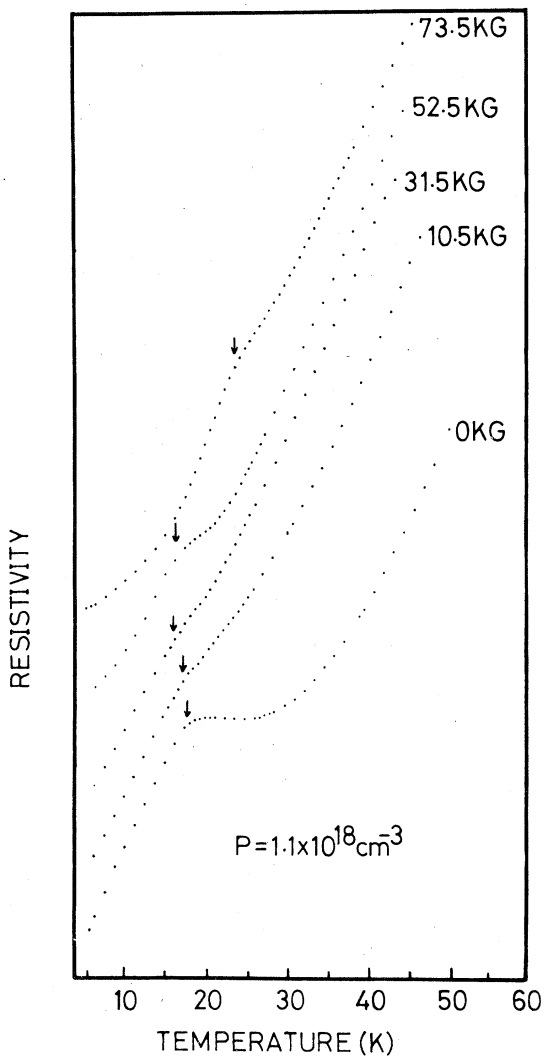

FIG. 5. Resistivity anomalies of $Pb_{1-x}Sn_xTe$ ($x=0.40$) under magnetic field (H is parallel to the ⟨100⟩ direction).

$$-\frac{2}{MNa^2}\sum_k |\Xi(k)|^2\frac{f(E_{ck})-f(E_{vk})}{E_{ck}-E_{vk}}$$

$$=K(W_0,H)-K(E_F,H)+\cdots \ , \quad (3.2)$$

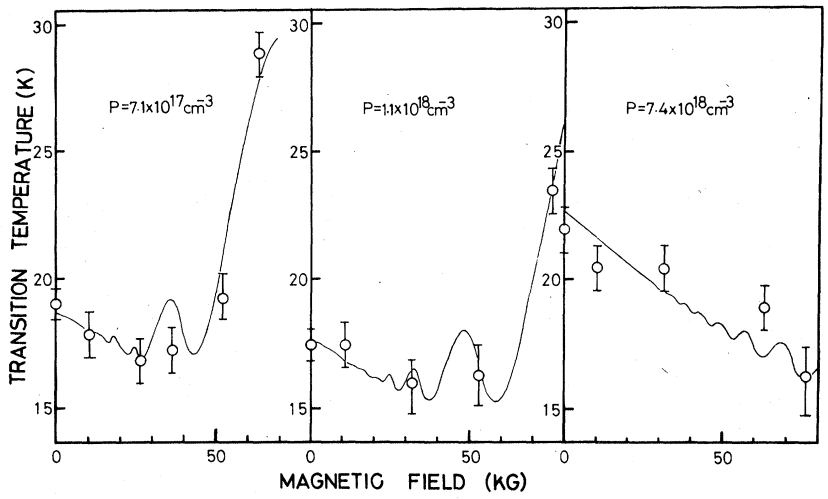

FIG. 6. Transition temperature vs magnetic field in $Pb_{1-x}Sn_xTe$ ($x=0.40$) with various carrier concentrations. The open circles are obtained from resistivity anomalies. The solid curves are obtained from the calculation (see text).

where the dots stand for the magnetic-field-nondependent term, with

$$K(E,H) = -\frac{2g}{MNa^2}\sum_{n,s}^{E_{ns}^c \le E}\int_0^{k_z^0} dk_z \frac{|\Xi(k)|^2 \rho_{ns}(H,k_z)}{E_{ns}^c(k_z,H) - E_{ns}^v(k_z,H)} ,$$

where g is the number of valleys ($g=4$), ρ_{ns} the joint density of states, W_0 the upper-limit energy of the summation (the "valley" width) and E_F the Fermi energy as schematically shown in Fig. 10. It is noted that both W_0 and E_F are functions of H, since we fix the carrier concentrations N_T and N_c under a magnetic field. The suffices n and s are the orbital and effective-spin quantum number, respectively.

Since the band gap of the PbTe-GeTe-SnTe system is very small (0–0.3 eV), the two-band model gives a fairly good approximation for near-band-edge structures. We give the dispersion relation of the two-band model in a magnetic field in Appendix B. The k-dependent deformation potential $\Xi(k)$ is expressed as (see Appendix A)

$$|\Xi(k)|^2 \equiv |\Xi(E(k))|^2 = \tfrac{1}{3}|\Xi^0|^2[1+2/(1+2\lambda)^2] \quad (3.3)$$

with

$$\Xi^0 = a\left|\langle\psi_{ck}|\frac{\partial v}{\partial u}|\psi_{vk}\rangle\right|$$

at the L point ($k=0$). Using Eqs. (3.3) and (B2), $K(E,H)$ in Eq. (3.2) becomes

$$K(E,H) = A\sum_{ns}^{E_{ns}\le E}(I_{ns}^a + I_{ns}^b) , \quad (3.4)$$

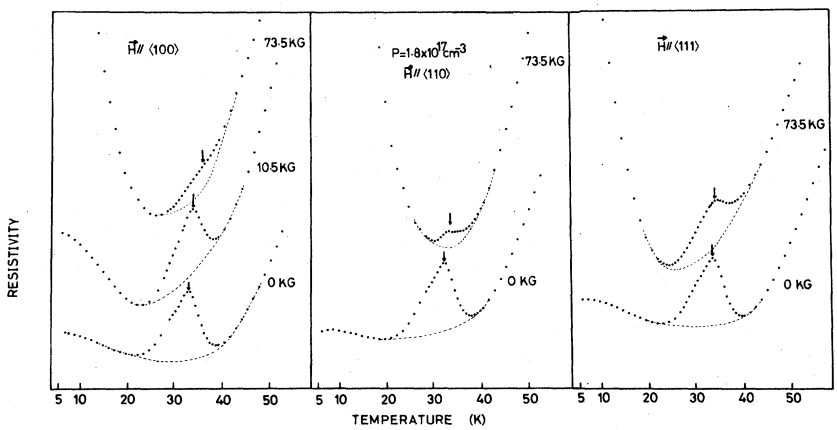

FIG. 7. Resistivity anomalies of low-carrier-concentration $Pb_{1-x}Ge_xTe$ ($x=0.01$) under magnetic field along the ⟨100⟩, ⟨110⟩, and ⟨111⟩ directions respectively.

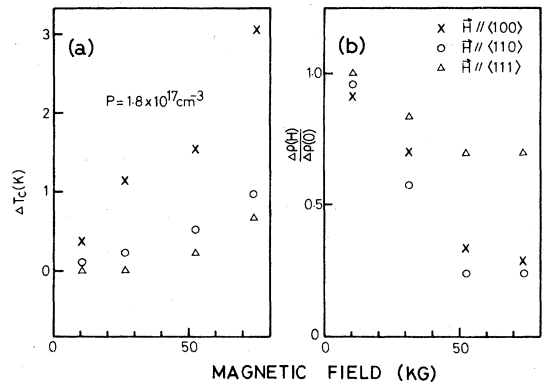

FIG. 8. (a) Transition-temperature shift vs magnetic field along the ⟨100⟩, ⟨110⟩, and ⟨111⟩ directions in $Pb_{1-x}Ge_xTe$ ($x=0.01$). (b) The peak height of the resistivity anomaly at T_c vs magnetic field along the ⟨100⟩, ⟨110⟩, and ⟨111⟩ directions.

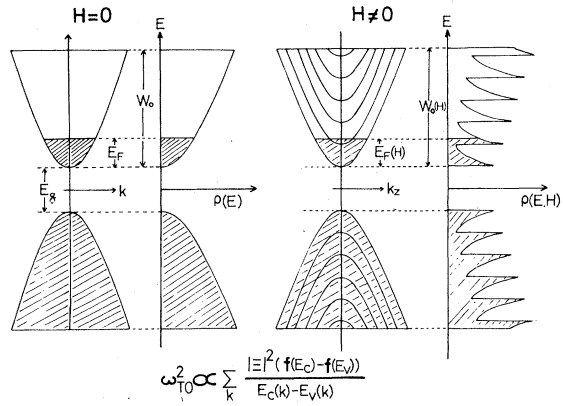

FIG. 10. Schematic illustration of the change in interband coupling due to a magnetic field [$\rho(E)$ is the density of states, W_0 the upper limit of the summation (the band width) and E_F the Fermi energy].

where

$$I_{ns}^{a}=\ln\{(1+2\lambda)+2[\lambda(\lambda+1)-C_{ns}]^{1/2}\}-\tfrac{1}{2}\ln(1+4C_{ns}) ,$$

$$I_{ns}^{b}=[\lambda(\lambda+1)-C_{ns}]^{-1/2}\left(\frac{2\lambda+1}{4C_{ns}+1}-\frac{1}{2\lambda+1}\right) ,$$

$$A=\frac{geH\sqrt{m_\rho}}{3\sqrt{2}\pi^2\hbar^2c\sqrt{E_g}MN}\left(\frac{\Xi^0}{a}\right)^2 ,$$

$$C_{ns}=\frac{\hbar\omega_c}{E_g}(n+\tfrac{1}{2}+\tfrac{1}{2}s) .$$

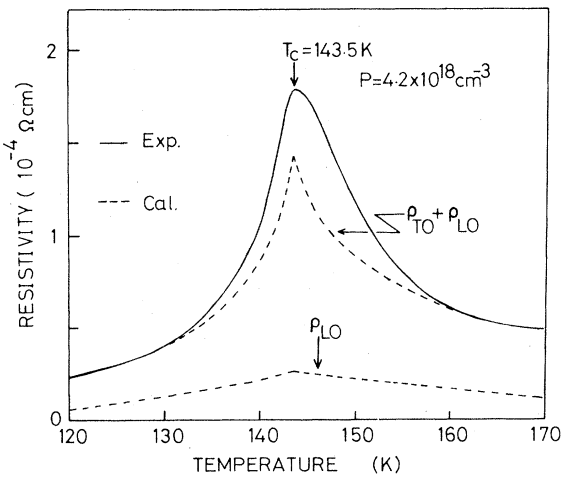

FIG. 9. Comparison of the resistivity anomaly in $Pb_{1-x}Ge_xTe$ ($x=0.055$) with calculation (Refs. 9 and 17). ρ_{TO} and ρ_{LO} are the resistivity anomalies due to the soft TO phonon and screened LO phonons (L^- modes), respectively.

The transition temperature T_c is defined as a zero of the TO-phonon frequency in Eq. (3.1), where the third term is replaced by Eq. (3.2). Since $\Delta T_c = T_c(H,N_c) - T_c(0,N_c) << \Theta$, we may approximate the second term in Eq. (3.1) as $\alpha(T_c)(T-T_0)$. It is easy to proceed to a p-type case by replacing N_c with a hole concentration P_c. The solid curves in Fig. 4 show the calculated magnetic-field dependence of T_c by the above model. The band parameters used in these calculations are as follows: $E_{g_\circ}=0.2$ eV, $m_\perp=0.026m_0$, $m_\parallel=0.26m_0$, $a=6.4$ Å, $M=1.31\times10^{-22}$ g, and W_0 is chosen to be large enough (~1 eV) not to influence the calculated results. The only adjustable parameter is $|\Xi^0|^2/\alpha$ which is estimated as 3.0×10^{-20} eV^2 sec^2 K rad^{-2} for $x=0.01$ and 2.0×10^{-20} eV^2 sec^2 K rad^{-2} for $x=0.015$. The agreement between the calculations and the experiments is fairly good in spite of the only one parameter used in the calculations. The temperature coefficient $\alpha(T_c)$ is smaller than the high-temperature-limit value α_∞ owing to the Bose-Einstein distribution of phonons. The coefficient $\alpha(T_c)$ is about $0.4\alpha_\infty$ for $T_c=30$ K ($x=0.01$) and about $0.66\alpha_\infty$ for $T_c=50$ K ($x=0.015$), which are deduced from Raman scattering ($\Theta=145$ K).[24] The experimental values of α_∞ for $Pb_{1-x}Ge_xTe$ ($0\leq x\leq0.05$) spread from 0.32×10^{23} rad^2 sec^{-2} K^{-1} to 1.7×10^{23} rad^2 sec^{-2} K^{-1}, which values are determined from neutron scattering,[12] microwave magnetoplasma reflection,[19] far-infrared reflection,[25] and Raman scattering.[24] The interband optical deformation potential at the band edge, Ξ^0, is 20–45 eV for $x=0.01$ and 21–48 eV for $x=0.015$, respectively. The values are comparable to 21 eV as estimated by a fitting with a resistivity anomaly in Fig. 9 (Ref. 8) and 24 eV as deduced from the minimum band-gap increment below T_c.[26]

Since the band gap is very small (~25 meV) in

$Pb_{1-x}Sn_xTe$ ($x=0.4$, 20 K) compared with $Pb_{1-x}Ge_xTe$, a larger effect on T_c is expected. The solid curves in Fig. 6 are calculated by the above-mentioned method on assuming a magnetic-field dependence of the band gap of the form $E_g = E_g^0 + \beta H$. Here β is a magnetic-field coefficient. The adjustable parameters are now $|\Xi^0|^2/\alpha$ and β. These are determined by a fitting procedure with the experimental results for the sample ($p = 1.1 \times 10^{18}$ cm^{-3}) in Fig. 6. The band-edge parameters used in this calculation are as follows: $E_g^0 = 25$ meV, $m_\perp = 0.0032 m_0$, and $m_\parallel = 0.032 m_0$. On using only two parameters, $|\Xi^0|^2/\alpha = 2.0 \times 10^{-19}$ eV^2 sec^2 K^2 rad^{-2} and $\beta = 3 \times 10^{-11}$ eV/G, the agreement between the calculated curves and the experimental points in different samples with different carrier concentrations is fairly good as shown in Fig. 6. The deformation potential Ξ^0 in this system is about 2.5 times as large as that for the $Pb_{1-x}Ge_xTe$ system, since α_∞ is comparable among them. Such a large value may not be realistic. So far we have not taken into account spin splitting which has not yet been well examined. If the spin splitting ($g\mu_B H$) is larger than the Landau splitting ($\hbar\omega_c$), the band-gap decrease with magnetic field causes a considerable enhancement of interband coupling and an increment in T_c owing to the very small band gap of the system. We may overestimate the value of Ξ^0, a part of which may be caused by the above-mentioned effect.

Finally, we will qualitatively discuss the magnetic-field directional dependence of the resistivity anomaly shown in Figs. 7 and 8. The T_c increment becomes increasingly smaller in the ⟨100⟩, ⟨110⟩, and ⟨111⟩ directions as shown in Fig. 8(a). We have the following two speculative explanations of this effect:

(i) The number of cyclotron lighter-mass valleys (g_L) which are responsible for the $\Delta T_c(H)$ decreases on going from the ⟨100⟩, to the ⟨110⟩, to the ⟨111⟩ direction, that is $g_L = 4$ for ⟨100⟩, $g_L = 2$ for the ⟨110⟩, and $g_L = 1$ for the ⟨111⟩ direction.

(ii) When, moreover, the magnetic field approaches the quantum limit, a carrier redistribution occurs: carriers of the heavy-mass valleys go into the light-mass valleys, since the density of states of a Landau subband of the light-mass valley is larger than that of the heavy-mass valley. Then the critical magnetic field satisfying the quantum limit in the light-mass valley increases and $\Delta T_c(H)$ decreases in the ⟨111⟩ and ⟨110⟩ directions, while there is no such carrier redistribution in the ⟨100⟩ direction.

The resistivity anomalies become small above the quantum-limit critical field. The speculations for this effect are as follows: the resistivity anomaly mainly comes from TO-phonon scattering (ρ_{TO}). The resistivity ρ_{TO} is proportional to the squared intraband matrix element which is proportional to k_F^2. When a magnetic field is higher than the quantum-limit critical field k_F (Fermi wave number) decreases rapidly and the resistivity anomaly decreases. The small effect in the ⟨111⟩ configuration cannot be explained at present, but there is a possibility that the quantum-limit field increases in this direction as discussed before.

So far we have presumed that the magnetic-field dependence of the peak position of the resistivity anomaly is due to the interband-electron–TO-phonon coupling. However, there might be another possibility that the TO-phonon frequency does not soften to zero but again hardens below T_c from nonzero frequency, under the magnetic field, and thus the effective T_c goes up. We have not analyzed such a possibility at present, but it would be necessary to consider such a mechanism hereafter.

IV. SUMMARY AND CONCLUDING REMARKS

The structural phase transition and its relation to electronic properties in PbTe-GeTe-SnTe alloy systems have been investigated by means of electrical-transport measurements in the absence and in the presence of a magnetic field near T_c. We summarize our experimental results and analyses as follows:

(a) The electrical-resistivity anomaly has been observed in $Pb_{1-x}Ge_xTe$ and $Pb_{1-x}Sn_xTe$ near T_c. The phenomena are attributed predominantly to the increase of carrier scattering due to the soft-optic mode. We determined T_c systematically in $Pb_{1-x}Ge_xTe$ up to 10 at.% Ge composition by the resistivity anomaly.

(b) The peak position of the resistivity anomaly (T_c) changes appreciably with application of a strong magnetic field in $Pb_{1-x}Ge_xTe$ ($x=0.01$ and 0.015) and $Pb_{1-x}Sn_xTe$ ($x=0.40$). The interband-electron–TO-phonon coupling model gives a semiquantitative explanation of the magnetic-field dependence of the peak position, assuming the peak position to be T_c. The value of the coupling constant in $Pb_{1-x}Ge_xTe$ ($x=0.01$ and 0.015) was estimated as $\Xi^0 = 10$–48 eV. We also found the magnetic-field directional dependence of the resistivity anomaly: $\Delta T_c(H)$ and its peak height.

It is desirable to carry out more experimental and theoretical studies on the relations between the phase transition and a magnetic field, for example, specific-heat or capacitance measurements under a strong magnetic field.

ACKNOWLEDGMENTS

We would like to express our sincere thanks to Professor Hajimu Kawamura for his constant encouragement and enlightening discussions. We wish to thank Dr. S. Katayama and Dr. S. Sugai for fruitful discussions. We would like to thank Dr. S. Nishikawa and S. Nishi for their kind supply of samples

and for discussions. We are very grateful to Professor S. Tanuma, Professor K. Kobayashi, and Dr. J. Nakahara for the use of the 150-kG superconducting magnet at the Institute of Solid State Physics (Tokyo) for performing a part of this work at magnetic fields above 90 kG. One of authors (K.M.) was supported in part by the Kurata Foundation and by the Grand-in-aid for Scientific Research (B) from the Ministry of Education, Science and Culture. One of the authors (S.T.) has been supported by Japan Society for the Promotion of Science.

APPENDIX A

By using the wave function for the L_6^+ and L_6^- levels ($L_{6\alpha}^+$, $L_{6\beta}^+$, $L_{6\alpha}^-$, and $L_{6\beta}^-$) which make up the conduction and valence bands (the two-band model), we can obtain the 4×4 Hamiltonian matrix in the $\vec{k}\cdot\vec{p}$ theory[27] as follows:

$$H=\begin{pmatrix} 0 & 0 & v_l k_z & v_\perp k_- \\ 0 & 0 & v_\perp k_+ & -v_l k_z \\ v_l k_z & v_\perp k_- & -E_g & 0 \\ v_\perp k_+ & -v_l k_z & 0 & -E_g \end{pmatrix} , \tag{A1}$$

where α and β denote the partners of a Kramers pair; $k_\pm = k_x \pm ik_y$; v_l and $v_\perp$ are the longitudinal- and transverse-velocity matrix elements between the conduction and valence bands, respectively. The eigenvalues E of the Hamiltonian in Eq. (A1) satisfy the following relation:

$$E(E+E_g)=v_l^2k_z^2+v_\perp^2k_+k_- . \tag{A2}$$

The eigenfunctions of the Hamiltonian in Eq. (A1) are given as follows:

$$\begin{aligned} \psi_\alpha^-(k) &= C[L_{6\alpha}^+ + A(P_zL_{6\alpha}^+ + P_+L_{6\beta}^+)] , \\ \psi_\beta^-(k) &= C[L_{6\beta}^- + A(P_-L_{6\alpha}^+ - P_zL_{6\beta}^+)] , \\ \psi_\alpha^+(k) &= C[L_{6\alpha}^+ - A(P_zL_{6\alpha}^- + P_+L_{6\beta}^-)] , \\ \psi_\beta^+(k) &= C[L_{6\beta}^+ + A(-P_-L_{6\alpha}^- + P_zL_{6\beta}^-)] , \end{aligned} \tag{A3}$$

where $A=1/(E+E_g)$, $P_z=v_lk_z$ and $P_\pm=v_\perp k_\pm$, and C is the normalization factor of the wave function given as $[(1+\lambda)/(1+2\lambda)]^{1/2}$, $\lambda=E/E_g$. The interband optical-deformation potential for a wave vector k is defined as

$$\begin{aligned} |\Xi(k)| = a\,|\langle\psi_\alpha^-(k)|\frac{\partial V}{\partial u}|\psi_\alpha^+(k)\rangle|^2 \\ + a\,|\langle\psi_\alpha^-(k)|\frac{\partial V}{\partial u}|\psi_\beta^+(k)\rangle|^2 , \end{aligned} \tag{A4}$$

where u is the internal coordinate of the optical phonon. When u is parallel to the z axis (trigonal axis),

$$|\Xi^z(k)|^2=|\Xi_0^z|^2\left[1-\frac{4P_+P_-}{(E_g+2E)^2}\right] , \tag{A5}$$

where

$$|\Xi_0^z|^2=a\,|\langle L_{6\alpha}^-|\frac{\partial V}{\partial u}|L_{6\alpha}^+\rangle|^2$$

is the deformation potential at the L point ($k=0$).

A similar result is obtained when u is perpendicular to the z axis, as follows:

$$|\Xi_\perp(k)|^2=|\Xi_\perp^0|^2\left[1-\frac{4(P_z^2+P_y^2)}{(E_g+2E)^2}\right] , \tag{A6}$$

where

$$|\Xi_\perp^0|^2=a\,|\langle L_{6\alpha}^-|\frac{\partial V}{\partial x}|L_{6\alpha}^+\rangle|^2, \quad P_y=v_\perp k_y .$$

Then we average $|\Xi(k)|^2$ over a surface at $E(k)=$const. The resulting deformation potential is

$$\begin{aligned} |\Xi(E)|^2 &\equiv \langle|\Xi(k)|^2\rangle_{\rm av} \\ &= \tfrac{1}{3}|\Xi^0|^2\left[1+\frac{2}{(1+2\lambda)^2}\right] . \end{aligned} \tag{A7}$$

APPENDIX B

The Hamiltonian matrix of the two-band model in zero magnetic field is given in Eq. (A1). When a magnetic field is applied ($\vec{H}\parallel\vec{z}'$ axis), the Hamiltonian is modified with $\vec{k}\rightarrow -i\vec{\nabla}-(e/c\hbar)\vec{A}$ in Eq. (A1), where $\vec{A}$ is the vector potential. The eigenvalue $[E_{ns}(k_{z'})]$ of the Hamiltonian is given as[28]

$$E_{ns}(k_{z'})[E_{ns}(k_{z'})+E_g]=E_g\left[(n+\tfrac{1}{2}+\tfrac{1}{2}s)\,\hbar\omega_c+\frac{\hbar^2k_{z'}^2}{2m_\rho}\right] ,$$

where

$$\begin{aligned} m_\rho &= \tfrac{1}{3}(2m_\perp+m_\parallel) = \tfrac{1}{3}E_g\left[\frac{1}{v_\perp^2}+\frac{1}{2v_l^2}\right] , \\ \omega_c &= \frac{eH}{m_cc} , \\ m_c &= m_\perp/(\tfrac{1}{3}+\tfrac{2}{3}m_\perp/m_\parallel)^{1/2} , \end{aligned} \tag{B1}$$

for $\vec{H}\parallel\langle100\rangle$.

Using the dispersion relation in Eq. (B1), we obtain the following relation used in Eq. (3.2):

$$\begin{aligned} \rho_{ns}(H,k_z) &= \frac{1}{(2\pi)^3}\frac{2\pi eH}{\hbar c}\frac{dk_z}{dE_{ns}(k_z)} \\ &= \frac{eH}{4\sqrt{2}\pi^2\hbar^2c}\frac{\sqrt{m_\rho}(1+2\lambda)}{[E(1+\lambda)-(n+\frac{1}{2}+\frac{1}{2}s)\,\hbar\omega_c]^{1/2}} \end{aligned}$$

$$E_{ns}^c(k_z,H)-E_{ns}^v(k_z,H)=E_g(1+2\lambda) , \tag{B2}$$

$$k_z^0=\frac{1}{\hbar}\{2m_\rho[E(1+\lambda)-(n+\tfrac{1}{2}+\tfrac{1}{2}s)\,\hbar\omega_c]\} ,$$

$$\lambda=\frac{E}{E_g} .$$

[1]I. Melngailis and T. C. Harman, in *Semiconductors and Semimetals,* edited by R. K. Willardson and A. C. Beer (Academic, New York, 1970), Vol. 5, p. 111.
[2]T. C. Harman, J. Phys. Chem. Solids 32, 363 (1971).
[3]T. C. Harman, J. Nonmetals 1, 183 (1973).
[4]D. C. Hohnke, H. Holloway, and S. Kaiser, J. Phys. Chem. Solids 33, 2053 (1972).
[5]S. G. Parker, J. E. Pinnel, and R. E. Johnson, J. Electron Mater. 3, 731 (1974).
[6]S. Sugai, K. Murase, and H. Kawamura, Solid State Commun. 23, 127 (1976).
[7]S. Sugai, K. Murase, S. Katayama, S. Takaoka, S. Nishi, and H. Kawamura, Solid State Commun. 24, 259 (1977).
[8]K. Murase, S. Sugai, S. Takaoka, and S. Katayama, in *Proceedings of the Thirteenth International Conference on the Physics of Semiconductors, Rome, 1976,* edited by F. G. Fumi (Marves, Rome, 1977), p. 305.
[9]H. Kawamura, K. Murase, S. Sugai, S. Takaoka, S. Nishikawa, S. Nishi, and S. Katayama, in *Proceedings of the International Conference on Lattice Dynamics, Paris, 1977,* edited by M. Balkanski (Flammarion, Paris, 1978), p. 658.
[10]K. L. I. Kobayashi, Y. Kato, Y. Katayama, and K. F. Komatsubara, Solid State Commun. 17, 875 (1975).
[11]K. L. I. Kobayashi, Y. Kato, and K. F. Komatsubara, Phys. Rev. Lett. 37, 772 (1976).
[12]H. A. Alperin, S. J. Pickart, and J. J. Phyne, Phys. Lett. A 40, 295 (1972).
[13]M. Iizumi, Y. Hamaguchi, K. F. Komatsubara, and Y. Kato, J. Phys. Soc. Jpn. 38, 443 (1975).
[14]L. Muldwar, J. Nonmetals 1, 177 (1973).
[15]R. T. Bate, D. L. Carter, and J. S. Wrobel, Phys. Rev. Lett. 25, 159 (1970).
[16]G. A. Antcliffe, R. T. Bate, and D. D. Buss, Solid State Commun. 13, 1003 (1973).
[17]S. Sugai, K. Murase, T. Tsuchihira, and H. Kawamura, J. Phys. Soc. Jpn. 47, 539 (1979).
[18]H. Kawamura, S. Nishikawa, and K. Murase, in *The Application of High Magnetic Field in Semiconductor Physics,* edited by J. F. Ryan (Oxford University, New York, 1978), p.170.
[19]S. Nishi, H. Kawamura, and K. Murase (unpublished).
[20]H. Kawamura, S. Katayama, S. Takano, and S. Hotta, Solid State Commun. 14, 259 (1974).
[21]N. Kristoffel and P. Konsin, Ferroelectrics 6, 3 (1973).
[22]K. L. I. Kobayashi, Y. Kato, N. Narita, K. F. Komatsubara, and M. Iizumi, in *Proceedings of the 14th International Conference on the Physics of Semiconductors, Edinburgh, 1978,* edited by B. L. H. Wilson, IOP Conf. Ser. No. 43 (IPPS, London, 1979), p. 441.
[23]S. Katayama, Solid State Commun. 19, 381 (1976).
[24]K. Murase, S. Sugai, T. Higuchi, S. Takaoka, T. Fukunaga, and H. Kawamura, in *Proceedings of the 14th International Conference on the Physics of Semiconductors, Edinburgh, 1978,* edited by B. L. H. Wilson, IOP Conf. Ser. No. 43 (IPPS, London, 1979), p. 437.
[25]W. Jantsch, G. Bauer, and A. Lopez-Otero, in *Proceedings of the 14th International Conference on the Physics of Semiconductors, Edinburgh, 1978,* edited by B. L. H. Wilson, IOP Conf. Ser. No. 43 (IPPS, London, 1979), p. 445.
[26]S. Takaoka and K. Murase (unpublished).
[27]D. L. Mitchell and R. F. Wallis, Phys. Rev. 151, 581 (1966).
[28]P. A. Wolff, J. Phys. Chem. Solids 25, 1057 (1964).